MDPI

Article

Investigations into the Photocatalytic and Antibacterial Activity of the Nitrogen-Annealed Titanium Oxide/Silver Structure

Jun-Kai Zhang, Kui-Shou You, Chen-Hao Huang, Pin-Jyun Shih and Day-Shan Liu *

Institute of Electro-Optical and Material Science, National Formosa University, Yunlin 632301, Taiwan
* Correspondence: dsliu@sunws.nfu.edu.tw; Tel.: +886-5-6315665

Abstract: In this study, a thin silver (Ag) layer was evaporated onto the anatase-titanium oxide (TiO_x) film. This structure was then annealed at various temperatures under nitrogen ambient to realize the Ag nanoparticles formed on the TiO_x surface. The photocatalytic activities of these TiO_x/Ag structures to decompose pollutants were determined from the rate constant while they were applied to decolorize the methylene blue (MB) solution in the presence of the UV light irradiation. According to the investigations on their surface bond configurations, the Ag nanoparticles were favorable for the transformation of the Ti^{4+} into the Ti^{3+} state in the TiO_x film, which functioned to prohibit the recombination of the photogenerated electron-hole-pairs on the TiO_x surface. The exposed TiO_x surface distributed over the 500 °C-annealed TiO_x/Ag structure performed an increase of about 40% in the rate constant compared to the individual TiO_x film. Moreover, this surface morphology composed of the anatase-TiO_x structures and Ag nanoparticles which was abundant in the oxide-related radical and Ag^+ chemical state also showed a perfect antibacterial efficiency against *Escherichia coli*.

Keywords: anatase-titanium oxide film; silver nanoparticles; photocatalytic activity; TiO_x/Ag structure; antibacterial efficiency

1. Introduction

In the past two decades, environmental pollution and global warming issues have garnered more attention. Regarding environmental pollution issues, the developments and research on the materials that decompose or reduce toxic gases and organic solvents emitted from industries have become a critical topic. Various technologies such as adsorption, electrocoagulation, ion exchange, and photocatalysis, have been applied for the removal of pollutants [1–4]. Among them, photocatalysis is the process that changes the rate of a chemical reaction by introducing electron-hole pairs (ehps) on the material's surface while it is exposed to light. The photogenerated ehps provides complex photooxidants such as hydroxyl radical (·OH), superoxide radical (·O_2^-), and hydrogen peroxide (H_2O_2) that exhibit strong oxidation for decomposing environmental pollutants [5]. The advantages of the photocatalysis over other technologies are such that the photogenerated ehps induced by the light irradiation on the photocatalyst are highly reliable and reproducible. Accordingly, investigations into photocatalytic materials as well as to strengthen its activity under light irradiation become one of the main projects of the current research. Regarding materials suitable for photocatalysts, titanium oxide (TiO_x) is the most popular candidate among the photocatalytic materials for being capable to decompose both the organic and inorganic pollutants due to its chemical stability, optical transparency at visible wavelength, high refractive index, non-toxic nature, and low cost. In general, the photocatalytic activity of the TiO_x material is typically affected by three factors: the crystalline structure, the specific surface area, and the recombination rate of the photo-generated ehps. In terms of the crystallinity, the formation of the anatase-TiO_x phase is crucial for exhibiting a high degree of the photocatalytic activity [6–8]. For the specific surface area, the processes to

construct a nanotextured surface or to fabricate nanospheric particles to enrich the reaction area exposed to the environmental pollutants are continually developed to improve the photocatalyticity of the TiO_x [9–12]. In addition to achieving the anatase crystallinity and enriching the specific surface area of the TiO_x film, the researchers also focused on separating or avoiding the recombination of the photo-generated ehps. Basically, there are two ways to prolong the existence of the photo-generated ehps in the TiO_x film: engineer the heterojunction structure with energy band discontinuity using metals or metal oxides, such as Ag, NiO, Cu_2O, SnO_2, WO_3, or ZnO, contact to the TiO_x film [13–17] or build up a defect state in the TiO_x energy bandgap by introducing extrinsic impurities, such as C, N, Pd, or F dopants, which may also be beneficial for allowing the onset of the photocatalyticity under visible wavelength irradiation [18–21]. In addition to enhancing the film's photocatalyticity for purifying environmental pollutants, researchers also are interested in activating extra functions of the contact materials or dopants in the TiO_x film to strengthen the resulting products in saving the troublesome problems of daily life. Considering the demands of daily life, efforts to ensure environmental sanitation and food safety are critical. A number of organic and inorganic materials have been employed as effective antimicrobial and/or antifungal agents to avoid the growth of viruses and bacteria [22–27]. They allow the excessive formation of reactive oxygen species, leading to oxidative stress and subsequently damaging or altering the cell structure and function. Among them, Ag is the most widely used material to fill this role not only because of its high biocidal activity against a broad range of microorganisms and viruses, but also because it can be simply nanosized via various processes to optimize the reaction efficiency [28–30]. To summarize the discussions mentioned thus far, TiO_x and Ag materials seem to be the best candidates for simultaneously resisting environmental pollution and infection. As a result, a TiO_x/Ag composite system with both quality photocatalytic and antibacterial activities had been announced. For instance, Sheikh et al. fabricated the TiO_2 nanofibers containing Ag nanoparticles using an electrospinning process. They found that the Ag nanoparticles with diameters of 5 to 10 nm were dispersed well in/on the TiO_2 nanofibers after calcining at a temperature of 600 °C in air ambient for one hour. The resulting inorganic TiO_2/Ag nanofibers showed good stability for biomedical applications [31]. Song et al. synthesized a TiO_x containing Ag nanoparticles onto the commercially Ti substrate using a reactive magnetron cosputtering system. The shape and size of the Ag nanoparticles dispersed in the TiO_x film affected by the power applied to the Ag target as well as the bias imposed on the substrate were investigated. The results indicated that the substrate bias caused an increase in the small-sized Ag nanoparticles while the metallic Ag content decreased and oxidized Ag increased as the power applied to the Ag target increased. The reduction in the size of the Ag nanoparticles and the fast ion release from the metallic Ag was responsible for optimizing the structure's antibacterial activity [32]. Bian et al. synthesized the $Ag/ZnO/AgO/TiO_2$ composite by chemical precipitation and hydrothermal method. They found that the existence of the AgO and Ag materials sandwiched by the ZnO and TiO_2 nanoparticles was facilitated for trapping and transferring the electron carriers, and thereby lengthening a longer lifetime of the photo-generated ehps. The resulting composite performed a kinetic rate constant doubly higher than that of the TiO_2 nanoparticles as it was employed to photocompose the rhodamine B (RhB) solution (R2-1, [33]). Deekshitha et al. addressed a novel liquid-based method to synthesize TiO_2 embedded AgO/Ag_2O nanocomposite. They demonstrated that the nanocomposite was activable both by UV and visible light irradiation due to the presence of the AgO and Ag_2O functioned to reduce the bandgap of the TiO_2 nanoparticles. The $AgO/Ag_2O@TiO_2$ nanocomposite performed highly crystalline with a bandgap energy of 1.75 eV without any calcination and almost completely degraded 100 ppm Reactive Blue (RB) 220 dye under visible lamp irradiation for 90 min (R2-3, [34]). Kacprzyńska-Gołacka et al. presented a TiO_2 + AgO coating using Ti and Ag targets through the reactive magnetron cosputtering technology. They discussed the size of the Ag/AgO nanoparticles and the percentage of the elemental composition of the TiO_2 + AgO coating, both of which were affected by the applied power on the targets.

The results demonstrated that the TiO_2 + AgO coating showed complete inhibition of the growth of *Escherichia coli* (*E. coli*) and *Bacillus subtilis*. Moreover, this coating structure also performed good photocatalytic activity when it was irradiated under both ultraviolet (UV) and visible lights [35]. Thukkaram et al. prepared an Ag nanoparticles-loaded TiO_2 coating on a Ti disc using plasma electrolytic oxidation. They studied the bactericidal efficiency of the oxidized TiO_2 coating affected by the concentration of the Ag nanoparticles in the electrolyte. The resulting coatings showed that the bactericidal effect could be enhanced by increasing the amounts of the Ag nanoparticles, which was helpful for releasing more Ag^+ ions into the bacterial solution [36].

Though the TiO_x/Ag system had been prepared by various technologies, studies on the TiO_x/Ag structures under thermally annealing process are rare reports. The annealing process affected on the photocatalytic and antibacterial activity of the TiO_x/Ag system as well as its thermal stability are both critical. Accordingly, in addition to the research to modify the photocatalytic surface of an anatase-TiO_x film with quality antibacterial features at the same time, an investigation on the structural evolution of the TiO_x/Ag structure influence by the annealing process also was carried out. For this purpose, a thin Ag layer as the antibacterial agent was evaporated onto the anatase-TiO_x film. To study the thermal process affected on the surface property, a post-annealing treatment under nitrogen ambient was then processed on the TiO_x/Ag structure and was expected to achieve the TiO_x surface decorated with Ag nanoparticles. Surface morphologies, chemical bond configurations, and crystalline structures of the as-deposited and annealed TiO_x/Ag structures were investigated. The corresponding photocatalytic and antibacterial activities were examined as the samples were used to decompose the methylene blue (MB) solution and sterilize *E. coli* activated by a UV lamp irradiation.

2. Material Preparation and Experimental Procedure

Hydro-oxygenated amorphous TiO_x films with a thickness of 200 nm were deposited onto silicon and quartz substrates (~10×10 mm^2) using the home-made plasma-enhanced chemical vapor deposition (PECVD) at a temperature of 200 °C. Titanium precursor vaporized from the titanium tetraisopropoxide [$Ti(OC_3H_7)_4$, TTIP] liquid was intermixed with pure oxygen gas in a mixbox and subsequently inlet to the deposition chamber. The deposition pressure, rf power, and gas flow rate of $TTIP/O_2$ gas mixture were controlled at 40 Pa, 100 W, and 120/20 sccm, respectively. The amorphous TiO_x films were then annealed at 600 °C for 30 min under ambient oxygen to result in the film crystallization with the anatase phase that possessed the optimal photocatalytic activity. A detailed setup for the PECVD system and evidence of the film crystallization have been described and reported elsewhere [37]. Following this, metallic Ag films with a thickness of 20 nm were thermally evaporated onto the crystalline TiO_x films surface. These TiO_x/Ag structures were then rapidly annealed at 300 °C, 400 °C, 500 °C, and 600 °C, respectively, under nitrogen ambient for 1 min. This annealing process was treated for realizing the formation of the Ag nanoparticles which was expected to enrich the heterojunction contact and enlarge the exposed surface of the TiO_x film and Ag layer. Another set of 20 nm-thick Ag films directly deposited onto the silicon and quartz were also prepared to study the evolution of the Au layers processed by the same RTA treatment.

The film thickness of the TiO_x film was measured using a surface profile system (Dektak 6M, Veeco, New York, NY, USA). Surface roughness and morphologies of the individual TiO_x and Ag films as well as the TiO_x/Ag structures were examined using an atomic force microscopy (AFM, DI-3100, Veeco, New York, NY, USA) and a field emission scanning electron microscope (FE-SEM, JSM-6700F, JEOL, Tokyo, Japan) operated at 3 kV. The corresponded optical transmittance of these samples was examined by a UV-Vis-NIR spectrophotometer (UVD 3500, Labomed, Inc., Los Angeles, CA, USA). The associated crystalline structures were conducted using a grazing incident x-ray diffractometer (GIXRD) at 30 kV and 30 mA using Cu $K_{\alpha 1}$ radiation (D-500, Siemens, Munich, Germany). X-ray photoelectron spectroscope (XPS) with monochromatic Al K_α radiation (PHI Quantera

SXM^{TM}, ULVAC-PHI, Kanagawa, Japan) were employed to examine the chemical bond configurations distributed over the structural surface. The energy scale of the spectrometer was calibrated using the core level of C 1s at 284.6 eV. The photocatalytic activities of the TiO$_x$ films incorporated with the thin Ag layers as well as the individual TiO$_x$ and Ag films were evaluated as they were applied to decolorize an aqueous MB solution under an UV lamp irradiation. The initial concentration of the MB solution was controlled at 20 mgL^{-1} with a pH value approximately of 7.0 ± 0.1. The photocatalysis on the MB solution was determined from the degradation of the solution concentration that were linked to the absorbance evolution at 665 nm measured using the UV-Vis-NIR spectrophotometer. The antibacterial activities were assessed with a plate-counting method used against *E. coli*. Microbiological tests were carried out as the samples were immersed into a nutrient broth, and the initial concentration of the *E. coli* bacteria was adjusted to 1.0×10^6 colony-forming unit (CFU)/mL by dilution. These specimens were then sterilized under the UV-lamp irradiation for 1 h. Subsequently, 0.1 mL of each dilution was taken and spread on the nutrient agar and then incubated at 37 °C for 24 h. The number of the bacterial colonies grown on the plates was counted (in CFU) and photographed. The UV-lamp (TLD 10 W/08, Philips, London, UK) employed to activate the specimens' photocatalyticity for decomposing the MB solution and to suppress the *E. coli* growth emitted the dominated wavelength of 365 nm (light ranging from 350 to 400 nm) with the power density controlled at 5 mW/cm^2.

3. Results and Discussions

Figure 1a–e show the surface roughness of the 20-nm thick Ag film directly deposited onto the silicon substrate and the films annealed at 300, 400, 500, and 600 °C under nitrogen ambient for 1 min, respectively, examined by AFM measurement. The as-deposited Ag film presented flat surface morphology with a root-mean-square surface roughness, R$_q$, of about 2.7 nm (Figure 1a). In contrast, the annealed films exhibited rough characteristics with a surface roughness greater than 10 nm. Moreover, the surface roughness decreased slightly to about 9.4 nm as the annealed temperature reached 600 °C (Figure 1e). The surface morphologies conducted from the FESEM observation for the Ag thin film before and after the thermal annealed treatment are given in Figure 2a–e. As shown in Figure 2a, the surface of the as-deposited Ag film exhibited island structures with closed wedge-like particles. For the surface morphologies of the annealed samples shown in Figure 2b–e, these wedge-like islands evolved into separated and round-like nanoparticles. The size of these Ag nanoparticles were abnormally distributed over the annealed surface. Moreover, the mean diameters of these nanoparticles calculated by the software ImageJ analysis were gradually decreased as the annealed temperature increased. A mean diameter of about 53 ± 14.5 nm was calculated as the Ag film annealed at 600 °C, while that of the nanoparticles annealed at 500 °C was 69 ± 16.3 nm. Incorporating the measurements of the surface roughness shown in Figure 1, the closed wedge-like islands observed from the as-deposited Ag film surface corresponded to a relatively smooth surface, while the separated Ag nanoparticles appearing on the annealed surface resulted in a marked increase in surface roughness. The optical transmittance and absorbance spectra of the as-deposited and annealed Ag thin films directly deposited onto the sapphire substrate are illustrated in Figure 3a and b, respectively. As can be seen from the optical transmittance of the as-deposited sample in Figure 3a, the opaque nature of the Ag film showed an optical transmittance lower than 40% around the visible wavelength (400~700 nm). For the samples annealed at 300, 400, and 500 °C, the transparency at the long and short wavelengths of the visible wavelength region was greatly improved, with a wide drop in the transmittance at around 450–600 nm. As the Ag film annealed at 600 °C, the optical transmittance around the visible wavelength was further improved to about 90% except for the drop of the optical transmittance to about 71% at the wavelength of 453 nm. Combined with the surface morphologies of the annealed samples shown in Figure 2b–e, the light leakage through the Ag nanoparticles boundaries was responsible for the optical transparency around

the visible wavelengths, while the transmittance drop at the visible wavelength could be ascribed to the localized surface plasmon (LSP) resonance emerging from the distributed Ag nanoparticles [38–40]. The position of the absorbance peaks shown in Figure 3b could be connected to the general size of the Ag nanoparticle distributed over the annealed samples, as quoted from the reports [41–43]. The blue-shift of the absorbance peak as the annealed temperature increased was linked to the general size of the Ag nanoparticles being decreased as the annealing temperature increased. Moreover, the decrease in the bandwidth of the absorbance peak also implied the improved homogeneity of the Ag nanoparticles [44,45]. As a consequence, the 600 °C-annealed sample that exhibited the narrowest absorbance bandwidth with the peak at 453 nm corresponded to the smallest and best homogenous nanoparticle size, as observed from Figure 2e.
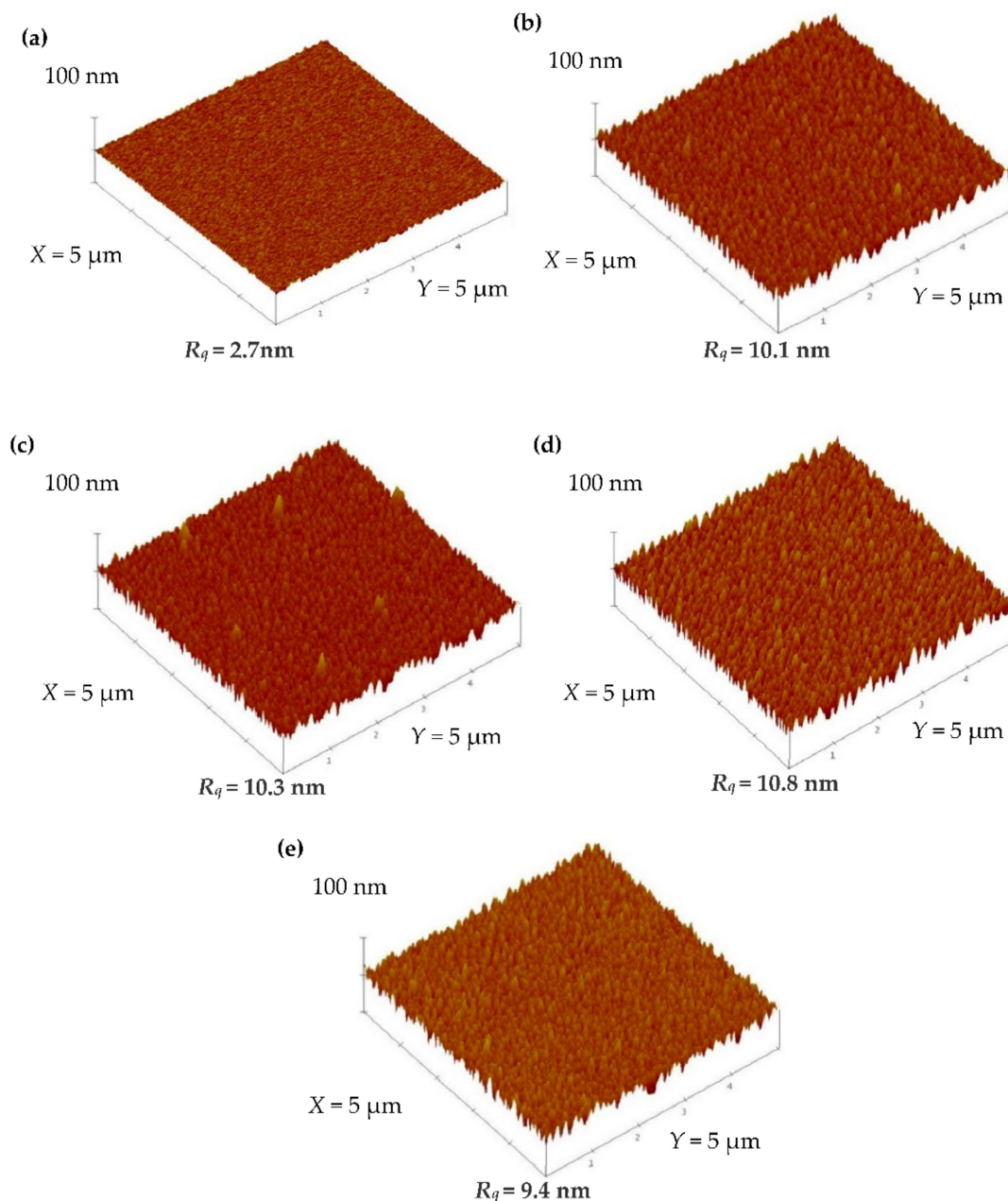
Figure 1. Surface roughness of (**a**) the as-deposited Ag film directly deposited onto the silicon substrate and the films annealed at (**b**) 300, (**c**) 400, (**d**) 500, and (**e**) 600 °C under nitrogen ambient for 1 min, examined by AFM measurement.
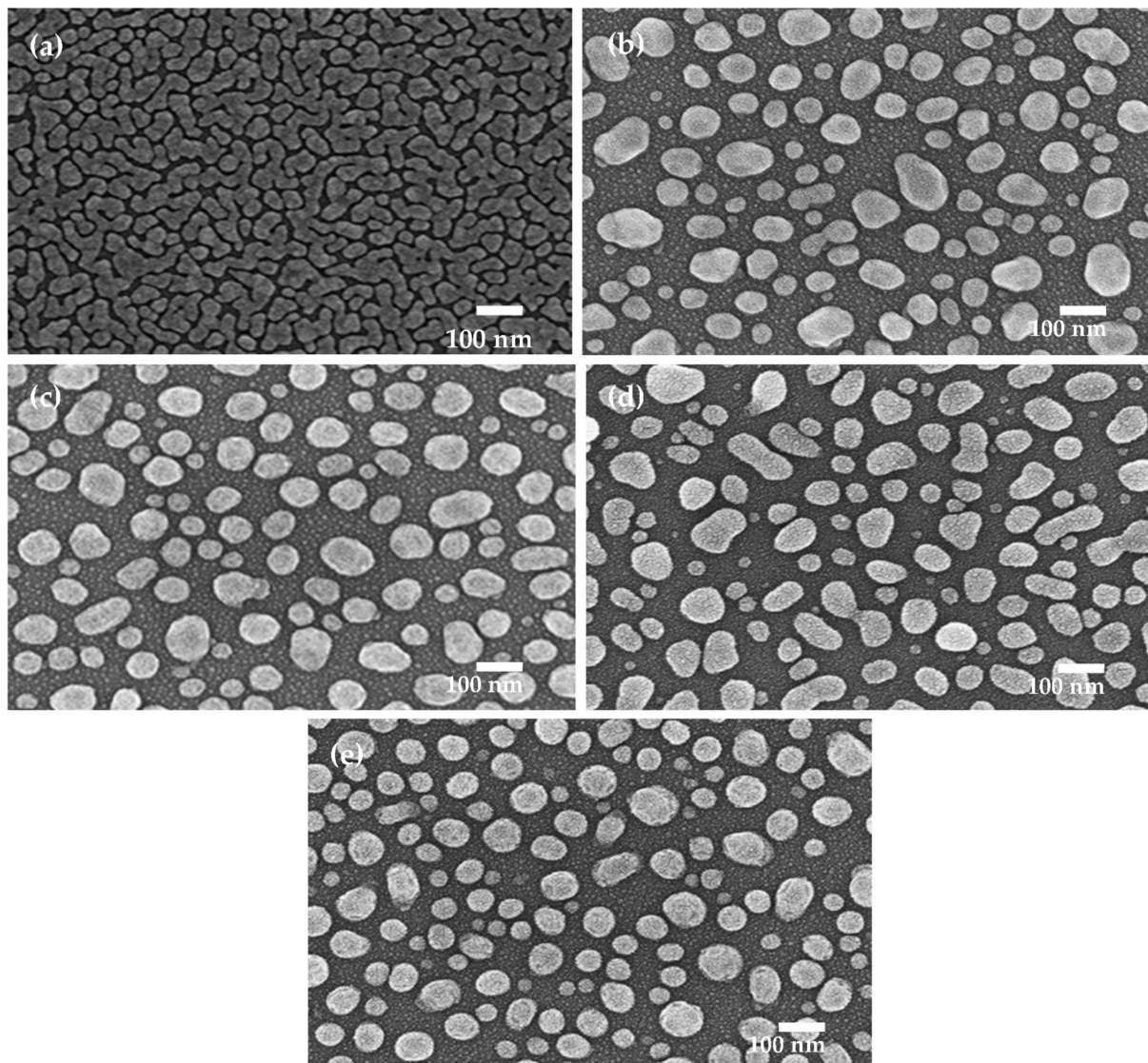
Figure 2. Surface morphologies of (**a**) the Ag film directly deposited onto the silicon substrate and the films annealed at (**b**) 300, (**c**) 400, (**d**) 500, and (**e**) 600 °C under nitrogen ambient for 1 min, conducted by FE-SEM observation.

According to these investigations, Ag nanoparticles were obtained from a thin Ag film treated by an adequate annealing process under nitrogen ambient. The specific surface area and optical transmittance around the visible wavelength of these Ag nanoparticles could be modified by controlling the annealed temperatures. This Ag layer with distinctive surface morphology and structure was then employed to alter the chemical and physical properties of the underlayer anatase-TiO_x film. Figure 4b–f show the surface roughness of the as-deposited TiO_x/Ag structure and the structures annealed at 300, 400, 500, and 600 °C under nitrogen ambient for 1 min, respectively (the surface roughness of the individual TiO_x film also is shown in Figure 4a for comparison). The PECVD-prepared TiO_x film, after annealing at 600 °C for 30 min under oxide ambient, possessed a surface roughness of about 4.2 nm. As an Ag layer was deposited onto the TiO_x film, the surface roughness was markedly increased to about 10.9 nm. A rougher surface that corresponded to an R_q value of about 18.0 nm was measured from the TiO_x/Ag structure annealed at 300 °C for 1 min under nitrogen ambient. As the annealed temperature reached 400 °C, the resulting TiO_x/Ag structure presented the roughest surface with an R_q value of about 18.5 nm (Figure 4d). The surface roughness of the TiO_x/Ag structure was then gradually decreased

to 16.2 and 15.5 nm while the annealed temperature was increased to 500 and 600 °C, respectively. The surface morphologies of the samples shown in Figure 4 are provided in Figure 5a–f. The grains distributed over the surface of the TiO_x film shown in Figure 5a were closely packed with visible boundaries. Interestingly, the Ag film deposited onto the TiO_x film (Figure 5b) was much different from the film directly deposited onto the silicon surface shown in Figure 2a. Nanoparticles and wedge-like islands were randomly and separately distributed over the TiO_x surface. This implied that the surface property of the TiO_x film facilitated the agglomeration of the Ag atoms to form islands and nanoparticles at a relatively low temperature. The appearance of the Ag islands and nanoparticles on the TiO_x film surface therefore resulted in a marked increase in the surface roughness (Figure 4a) compared to the Ag layer directed deposited onto the Si substrate. Unlike in the nanoparticles distributed over the 300 °C-annealed Ag film while being directly deposited onto the silicon substrate shown in Figure 2b, the density of the Ag nanoparticles distributed over the TiO_x surface under the same annealed temperature was obviously depressed, which might diffuse into the TiO_x film through the grain boundaries. A large area of the under-layered TiO_x film was thus observed from the surface morphologies of the 300 °C-annealed TiO_x/Ag structure (Figure 5c). The surface morphology combined with the scattered Ag nanoparticles and uneven TiO_x grains resulted in a rougher surface roughness (~18.0 nm) compared to the 300 °C-annealed Ag film on the silicon substrate (~10.1 nm). The density of the Ag nanoparticles distributed over the TiO_x surface decreased as the annealed temperature on the TiO_x/Ag structure increased. Figure 6 depicts the optical transmittance of the individual TiO_x film, the as-deposited TiO_x/Ag structure, and the structures annealed at 300, 400, 500, and 600 °C. The individual TiO_x film possessed an average transmittance higher than 90% around the visible wavelength, and then a sharp reduction in the near ultraviolet wavelengths was measured due to the absorption by the energy bandgap of the anatase-TiO_x structure. For an Ag layer deposited onto the TiO_x film, the resulting average optical transmittance markedly decreased to about 43% due to the injecting photons being obstructed by the Ag particles. The average optical transmittance was gradually increased as the annealed temperature on the TiO_x/Ag structure increased. An average optical transmittance of about 68% was measured from the structure annealed at the temperature of 600 °C. Considering the surface morphologies shown in Figure 5c–f, the increase in the transparency around visible wavelengths of these annealed TiO_x/Ag structures was ascribed to the decrease in the coverage of the Ag nanoparticles. Moreover, the size of the Ag nanoparticles distributed over the TiO_x film surface that caused the LSP phenomena was identified as one of the reasons for the depressions in the optical transmittance over the visible wavelengths. The crystalline phases of the as-deposited and annealed TiO_x/Ag structures as well as the individual TiO_x and Ag films conducted by the x-ray diffractometer measurement are illustrated in Figure 7. Two peaks identified as the anatase structure (denoted as "A" with the diffraction planes given in parentheses) according to JCPDS no.21-1272 could be observed from the XRD spectrum of the TiO_x film [46]. The crystalline phase of A(101) was the preferred growth orientation in this anatase TiO_x film. For the thin Ag layer, only a weak signal denoted as the Ag (111) that matched with the face centered cubic (fcc) structure according to the JCPDS no.04-0783 could be observed [47]. As this thin Ag layer was deposited onto the TiO_x film, no significant peaks other than these peaks belonging to the anatase-TiO_x and Ag phases appeared in the XRD spectrum. The XRD spectra of these annealed TiO_x/Ag structures also showed similar diffraction peaks to those of the as-deposited structure, indicating that little chemical reaction occurred between the TiO_x and Ag materials during the Ag layer deposition and the subsequent annealed treatment. In addition, there was no evidence of the Ag atoms doped into the TiO_x matrix as the peak position of the A(101) phase in the XRD spectra of the TiO_x/Ag structures was almost the same as the individual TiO_x film. Regarding crystallinity of the Ag layer while deposited onto the TiO_x film, the crystal size was smaller than that of the layer directly deposited onto the silicon substrate as derived from the full width of the half maximum (FWHM) of the Ag(111) peak according

to the Scherrer formula. Though the metal state was the dominated composition in the Ag nanoparticles, it still could not be ruled out the possibility of the oxidized state coexisted in the nanoparticles since the Ag_2O signal might be overlapped by the Ag (111) peak. As a consequence, XPS analysis was carried out to investigate the compositions of the Ti, O, and Ag elements. The binding energy spectra related to the Ag 3d, Ti 2p, and O 1s core levels, as illustrated in Figure 8a–c, respectively, are provided to further elucidate the evolution of the chemical bond configurations on the surface of the as-deposited and 500 °C-annealed TiO_x/Ag structures (the individual Ag and TiO_x films are also given as comparisons). Two distinctive peaks that were denoted as Ag $3d_{5/2}$ and Ag $3d_{3/2}$, with approximately 6 eV difference in the binding energy, could be seen in Figure 8a. The peak of the Ag $3d_{5/2}$ binding energy emerged from both the Ag film deposited onto the silicon and TiO_x surface both was approximately 368.2 eV, whereas the TiO_x/Ag structure annealed at 500 °C caused a shift in the binding energy at 367.8 eV. According to previous literatures, the shift in the binding energy observed from the surface of the annealed TiO_x/Ag structure was ascribed to the evolution on the chemical stat from the metallic Ag^0 signal to the oxidized Ag^+ state [48–51]. In the Ti 2p spectrum (Figure 8b), two peaks assigned as Ti $2p_{3/2}$ and Ti $2p_{1/2}$, with a binding energy difference of 5.6 eV, were also observed. Compared to the individual TiO_x film, the Ti $2p_{3/2}$ binding energy shifted from 458.9 eV to 458.6 eV as the TiO_x film was covered by a thin Ag layer. This peak further shifted to 458.2 eV while the TiO_x/Ag structure annealed at 500 °C. The shift of the Ti $2p_{3/2}$ single toward a lower binding energy could be related to the increased formation of the titanium atoms from the Ti^{4+} to the reduced Ti^{3+} state upon the Ag layered deposition and the structural annealed treatment, as referred to the reports [52–56]. For the O 1s spectrum shown in Figure 8c, the surface of the individual TiO_x film emerged a somewhat asymmetrical signal at a binding energy of about 530.0 eV, with a tail extending to the high binding energy. As an Ag layer deposited onto the TiO_x film, the O 1s signal emerged from the surface was drastically depressed with a weak peak at about 531.1 eV. The O 1s signal measured from the surface of the 500 °C-annealed TiO_x/Ag structure was obviously enhanced with a peak of approximatively at 529.2 eV and a notable shoulder extending to the higher binding energy. Considering the reports on the oxidized states of the titanium and silver atoms, this signal emerging from the surface of the 500 °C-annealed TiO_x/Ag structure could be linked to a combination of the oxygen species of the Ag-O (~528.9 eV), Ti-O (~529.7 eV), terminal hydroxyl (~530.8 eV), surface carbonate-like admixtures (~531.7 eV), and adsorbed water [50,51,55–60]. According to the studies on the crystallinity and surface bond configurations of the TiO_x/Ag structure, it demonstrated that, although there was little chemical reaction between the TiO_x film and Ag layer, the surface property combined with the oxidized state evolution from Ti^{4+} to Ti^{3+} in Ti-O bonds and the metallic (Ag^0)/oxidized Ag (Ag^+) states was measured from the 500 °C-annealed sample.
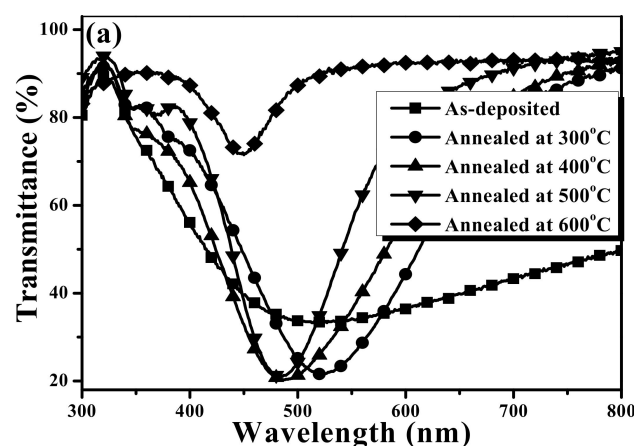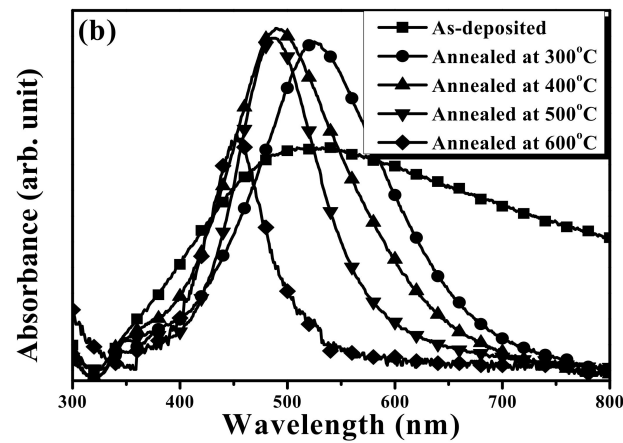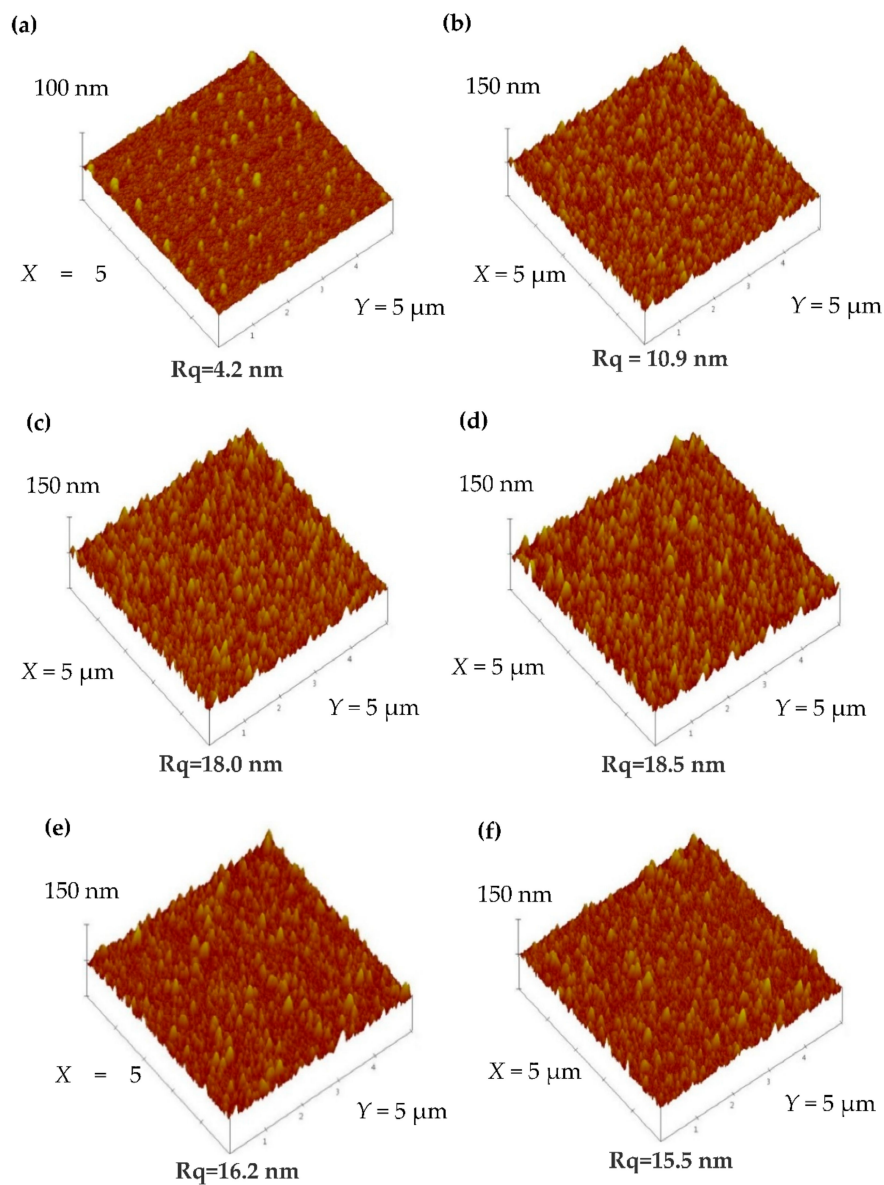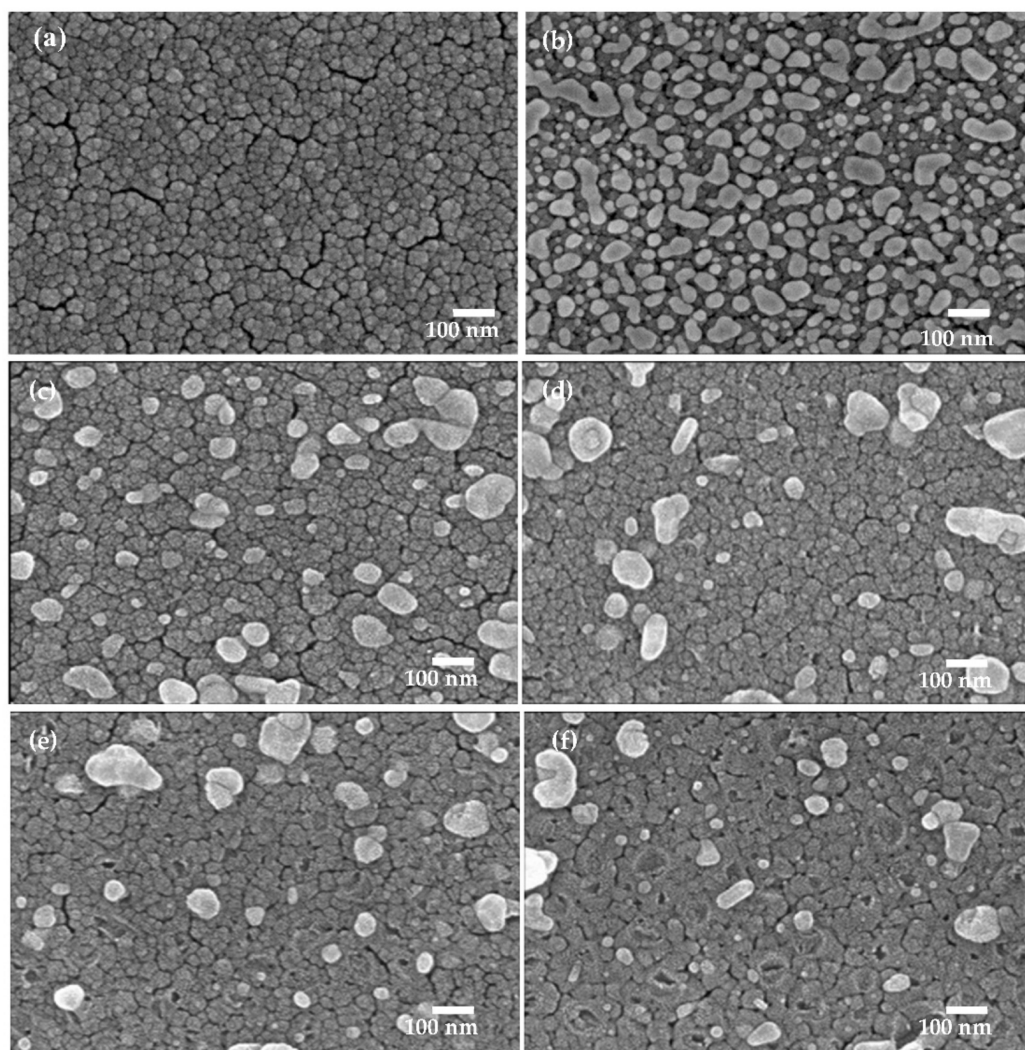

Figure 3. *Cont.*

Figure 3. (**a**) Optical transmittance and (**b**) absorbance spectra of the as-deposited and annealed Ag films directly deposited onto the sapphire substrate.

Figure 4. Surface roughness of (**a**) the TiO_x film, (**b**) the as-deposited TiO_x/Ag structure, and the structures annealed at (**c**) 300, (**d**) 400, (**e**) 500, and (**f**) 600 °C under nitrogen ambient for 1 min, examined by AFM.

Figure 5. Surface morphologies of (**a**) the TiO_x film, (**b**) the as-deposited TiO_x/Ag structure, and the structures annealed at (**c**) 300, (**d**) 400, (**e**) 500, and (**f**) 600 °C under nitrogen ambient for 1 min, conducted by FE-SEM observation.
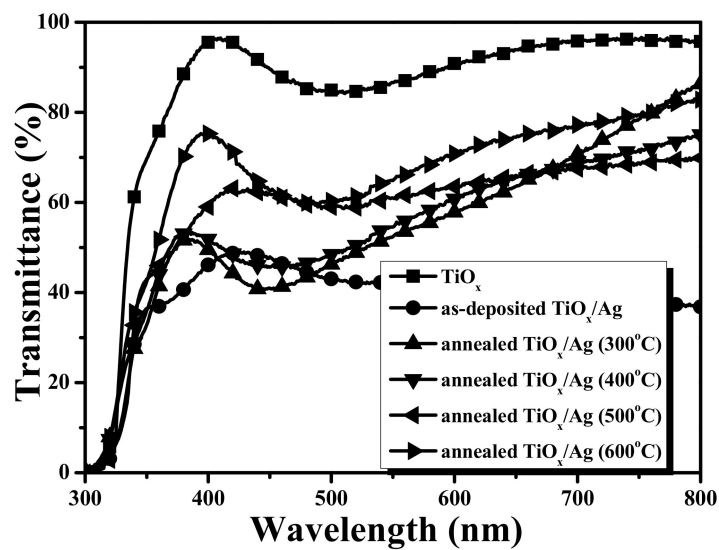
Figure 6. Optical transmittance of the as-deposited and annealed TiO_x/Ag structures (optical transmittance of the TiO_x film also is shown as a comparison).

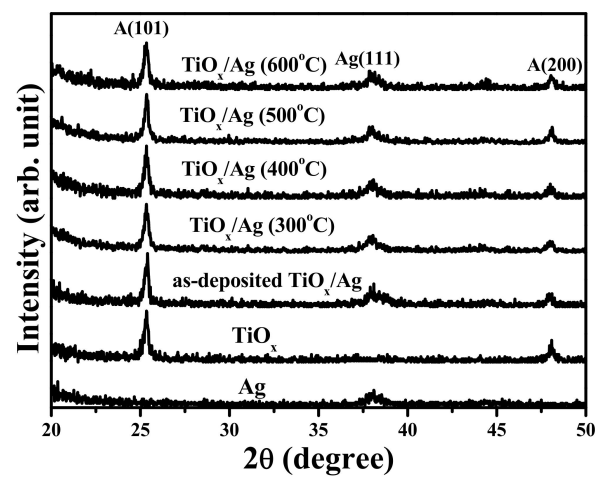**Figure 7.** XRD spectra of the as-deposited and annealed TiO_x/Ag structures as well as the TiO_x and Ag films.
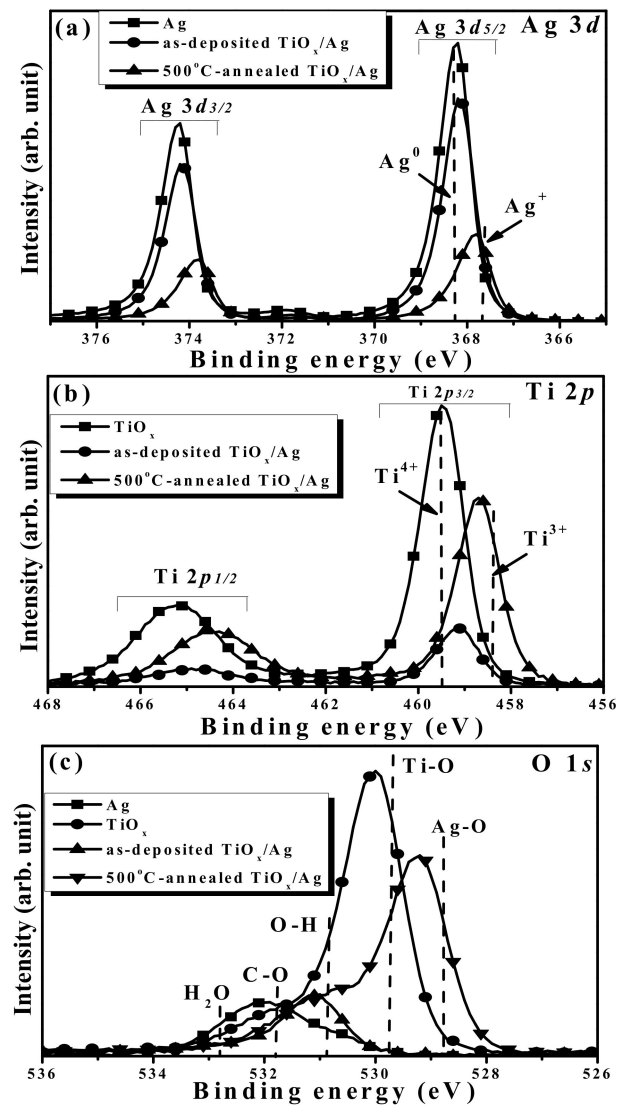

Figure 8. Binding energy spectra of the (**a**) Ag 3d, (**b**) Ti 2p, and (**c**) O 1s core levels measured from the surface of the as-deposited and 500 °C-annealed TiO_x/Ag structures (the individual Ag and TiO_x films are also given as comparisons).

The concentration evolution of the MB solution decomposed by using the TiO_x film, thin Ag layer, and the as-deposited and annealed TiO_x/Ag structures under the UV light irradiation are illustrated in Figure 9a (the change in the concentration of the MB solution directly irradiated by the UV light is also provided as a comparison). The degree of the photocatalytic activity for these samples, determined in terms of the rate constant, is summarized in Table 1. The rate constant, *k*, is derived by fitting the curves in Figure 9a, using the following relationship [61]:

$$\ln(C/C_0) = kt \tag{1}$$

where *C* and C_0 are the concentrations of the MB solution under UV light irradiation time of *t* = 0 and *t*, respectively. As can be seen in this figure, the degradation of the MB solution induced by the UV light irradiation was significantly enhanced by introducing a TiO_x film, while the Ag layer was almost useless in strengthening the decomposition of the MB solution under UV light irradiation. The corresponding rate constant derived from the curve of the Ag layer (~0.0029 min^{-1}) was only a little higher than that of the curve derived from the MB solution (~0.0027 min^{-1}). In contrast to the Ag layer, a nearly quadruple increase in the rate constant (~0.0102 min^{-1}) was obtained from the MB solution decomposed by the TiO_x film under UV light irradiation. Interestingly, although the Ag layer individually was inactive in decomposing the MB solution, the as-deposited TiO_x/Ag structure irradiated by the UV light took effect and corresponded to a rate constant of about 0.0110 min^{-1}. As referred to in Figure 5b, the areas of the TiO_x film uncovered by the Ag layer might be responsible for the activation regions to decomposed the MB solution. Moreover, the appearance of the Ti^{3+} state on the structural surface induced by the Ag ions which functioned to suppress the recombination of the photogenerated ehps resulted in a rate constant being higher than that of the individual TiO_x film. For the same reason, the extensive reaction area of the TiO_x surface that was abundant in the Ti^{3+} chemical state for the 500 °C-annealed TiO_x/Ag structure, as demonstrated in Figures 5e and 8b, resulted in the significant enhancement on the photodecomposition to the MB solution at a rate constant of about 0.0141 min^{-1}. The degree of the rate constant for the TiO_x/Ag nanoparticles system evaluated from decolorizing the MB solution was comparable to that of the photocatalytic materials under sunlight or UV light irradiation, as quoted from the reports [62–66]. The photo-excited current responses as the transient of the UV light irradiation for the TiO_x film and 500 °C-annealed TiO_x/Ag structure are given in Figure 9b. According to the cycles of the on-off current transient, the photocatalysis of the samples under UV light irradiation was reproducible and reliable. Under the same irradiation power, the degree of the photo-induced current from the TiO_x/Ag structure was much higher than that of the TiO_x film, indicating that the TiO_x/Ag structure was beneficial for the separation of the photo-generated ehps. Moreover, the longer transient time determined from the highest photo-excited current to the dark current was obtained from the TiO_x/Ag structure (8 min) as compared to that of the TiO_x film (4 min). This also showed evidence of the recombination rate of the photo-generated ehps could be effectively alleviated in the TiO_x/Ag structure. The mechanism responsible for the separation of the photo-generated ehps is ascribed to the difference of the electron affinity between the TiO_x and Ag interface which causes the photo-generated electrons flow to the Ag surface while the photo-generated holes stay at the TiO_x side [33]. In addition, the presence of the Ag nanoparticles that accept oxygen atoms from the TiO_x matrix to result in the reduction of the oxidized state of Ti^{4+} to Ti^{3+} is also facilitated for capturing the photo-generated hole on the TiO_x surface [46]. Those photo-generated ehps react with the adsorbed O_2 and H_2O and subsequently produce free radicals of $\cdot OH$ and $\cdot O_2^-$, thereby decomposing the MB solution into nontoxic products [62]. Figure 10a–d show the photographs of the *E. coli* bacterial colonies on the nutrient agar after a 24 h incubation period using the UV light-activated as-deposited and annealed TiO_x/Ag structure as well as using the TiO_x film and thin Ag layer, respectively. The number of the bacterial colonies counted from the plate, as shown in Figure 10a,b, was about $(230 \pm 11) \times 10^3$ CFU/mL and $(215 \pm 6) \times 10^3$ CFU/mL,

respectively. As the *E. coli* was sterilized using the as-deposited TiO$_x$/Ag structure, the number of the bacteria grown on the plate significant decreased to $(133 \pm 8) \times 10^3$ CFU/mL. Eventually, the bacteria were almost absent on the plate as they were sterilized by using the 500 °C-annealed TiO$_x$/Ag structure. The reduction percentage, *R*, of the bacteria growth on the plate was calculated using the following equation [67]:

$$R = [(A - B)/A] \times 100\% \tag{2}$$

where *A* is the number of the bacterial colonies counted from the *E. coli* directly sterilized by the UV-lamp irradiation ($\sim 382 \pm 16 \times 10^3$ CFU/mL), and *B* is the number of the bacterial colonies counted from the plate treated by the samples. The reduction percentages of these plates shown in Figure 10 are given in Table 1. The reduction percentages of the *E. coli* using the Ag and TiO$_x$ films were about 44% and 40 %, respectively. The sterilized activities conducted from the Ag layer was ascribed to the release of the Ag$^+$ ion could bind the proteins of the bacteria to cause the increase of the cellular oxidative stress, thereby resulting in the protein deactivation [68]. On the other hand, the photo-generated ehps on the TiO$_x$ surface could produce active radicals of ·OH and ·O$_2^-$ to interact with cell walls and rupture bacterial cell membranes [69]. Accordingly, the TiO$_x$ film incorporating a thin Ag layer resulted in the antibacterial efficiency against *E. coli*, with a higher reduction percentage of 65%. Moreover, the achievement of the TiO$_x$ film surface decorated with the Ag nanoparticles which was abundant in the Ag$^+$ and oxidant radical such as ·OH and ·O$_2^-$ on the surface as it was annealed at a temperature of 500 °C for 1 min under nitrogen ambient could completely inhibit the growth of the *E. coli* bacteria.

Table 1. Rate constant (*k*) and reduction percentage (*R*) of the Ag, TiO$_x$, as-deposited TiO$_x$/Ag, and 500 °C-annealed TiO$_x$/Ag samples.

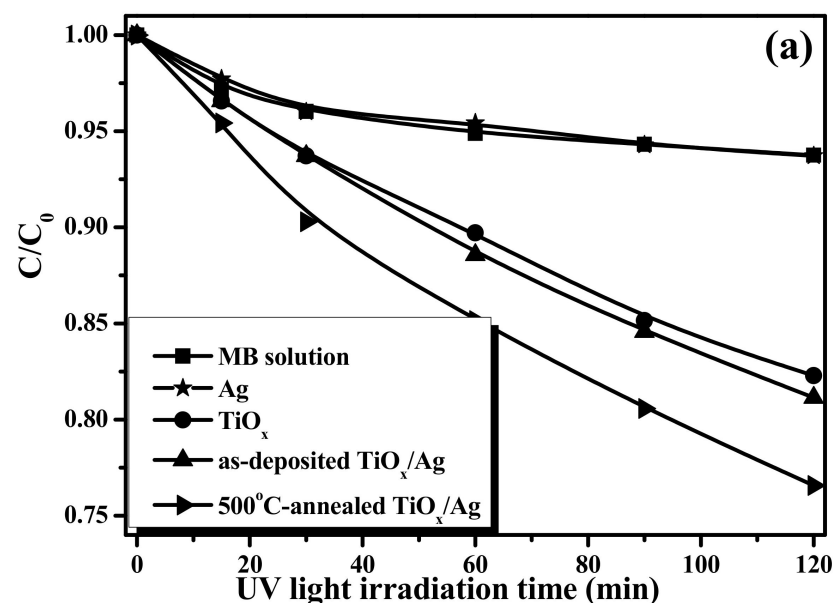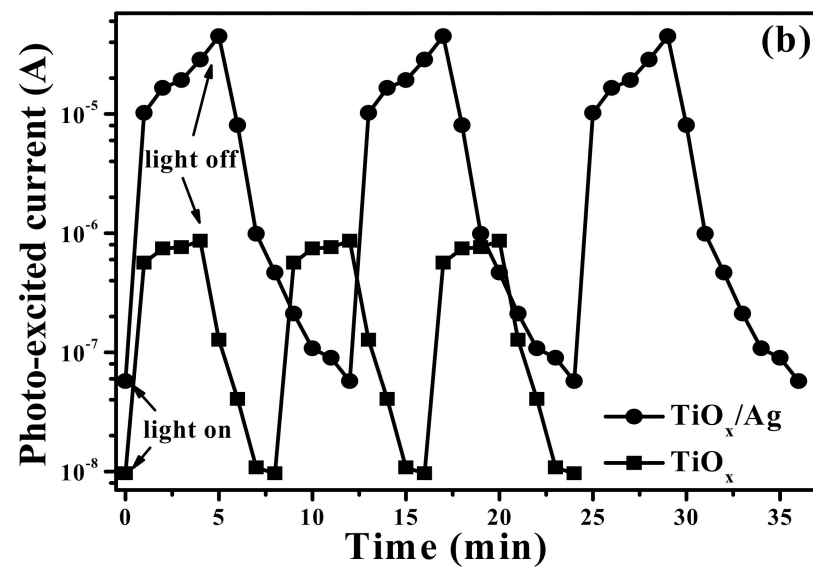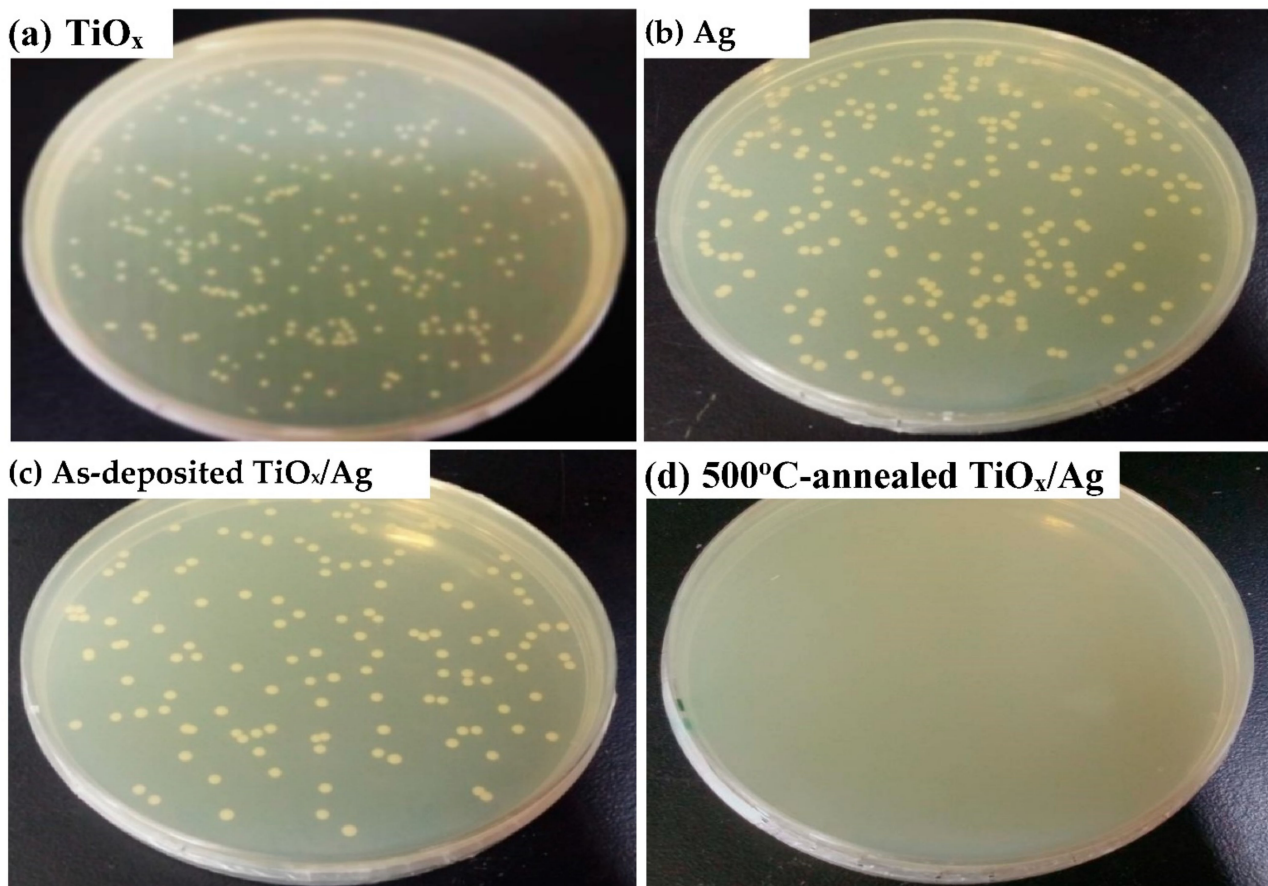|	Ag	TiO$_x$	As-Deposited TiO$_x$/Ag	500 °C-Annealed TiO$_x$/Ag
k (min^{-1})	0.0029	0.0102	0.0110	0.0141
R (%)	44	40	65	100

Figure 9. *Cont.*

Figure 9. (**a**) Concentration evolution of the MB solution decomposed by using the TiO$_x$ film, thin Ag layer, and the as-deposited and annealed TiO$_x$/Ag structures under the UV light irradiation (the change in the concentration of the MB solution directly irradiated by the UV light is also provided as a comparison); (**b**) the photo-excited current responses as the transient of the UV light irradiation for the TiO$_x$ film and 500 °C–annealed TiO$_x$/Ag structure.

Figure 10. Photographs of the *E. coli* bacterial colonies on the nutrient agar after a 24 h incubation period that are sterilized using the (**a**) TiO$_x$, (**b**) Ag, (**c**) as-deposited TiO$_x$/Ag and (**d**) annealed TiO$_x$/Ag samples under the UV-lamp irradiation for 1 h.

4. Conclusions

The surface property of the TiO$_x$/Ag structure activated by a UV-lamp irradiation was investigated. A thin Ag layer deposited onto the anatase-TiO$_x$ film exhibited an uneven surface morphology with separated Ag nanoparticles and wedge-liked islands. This TiO$_x$/Ag structure annealed under nitrogen ambient caused the agglomeration and diffusion of the Ag atoms, resulting in extensive TiO$_x$ film being exposed on the surface. The chemical bond configurations associated with the metallic Ag^0 to oxidized Ag$^+$ and the reduced oxidized states of Ti^{4+} to Ti^{3+}, which were beneficial to separate the photogenerated ehps and suppress the recombination rate, were observed from the composite surface of the Ag nanoparticles and TiO$_x$ layer. The decomposition efficiency of the MB solution under UV-lamp irradiation was apparently improved incorporating with the TiO$_x$/Ag structure annealed at a temperature of 500 °C under nitrogen ambient for 1 min. The derived rate constant (~0.0141 min^{-1}) was about 40% higher than that of the rate constant as incorporated with only the TiO$_x$ film (~0.0102 min^{-1}). This TiO$_x$ film decorated by the Ag nanoparticles which produced hydroxyl radicals and reactive oxygen species on the TiO$_x$ surface under UV light irradiation as well as the release of the Ag$^+$ ions from the nanoparticles resulted in the enhanced inhibition of the growth of the *E. coli*. The reduction percentage against the *E. coli* using the as-deposited TiO$_x$/Ag structure was about 65%, whereas a perfect antibacterial efficiency (the reduction percentage reaches 100%) was achieved by using the 500 °C-annealed sample. Such a surface property possessed excellent photo-activated properties to decompose pollutants and inhibit the growth of the microbial organisms, providing promising high-value products for the purification demands related to environmental pollution and sanitation.

Author Contributions: Conceptualization, D.-S.L.; Resource, D.-S.L.; Methodology, K.-S.Y.; Formal analysis, P.-J.S.; Investigation, P.-J.S., J.-K.Z. and C.-H.H.; Writing-original draft, J.-K.Z. and C.-H.H.; Writing-review & editing, D.-S.L. All authors have read and agreed to the published version of the manuscript.

Institutional Review Board Statement: Not applicable.

Informed Consent Statement: Not applicable.

Data Availability Statement: Not applicable.

Conflicts of Interest: The authors declare that there are no conflict of interest regarding the publication of this paper.

References

1. Sharma, G.; Pathania, D.; Naushad, M.; Kothiyal, N.C. Fabrication, characterization and antimicrobial activity of polyaniline Th(IV) tungstomolybdophosphate nanocomposite material: Efficient removal of toxic metal ions from water. *Chem. Engineer. J.* **2014**, *251*, 413–421. [CrossRef]
2. Akbarnejad, S.; Amooey, A.A.; Ghasemi, S. High effective adsorption of acid fuchsin dye using magnetic biodegradable polymer-based nanocomposite from aqueous solutions. *Microchem. J.* **2019**, *149*, 103966. [CrossRef]
3. Babu, D.S.; Singh, T.S.A.; Nidheesh, P.V.; Kumar, M.S. Industrial wastewater treatment by electrocoagulation process. *Sep. Sci. Technol.* **2020**, *55*, 3195–3227. [CrossRef]
4. Erusappan, E.; Thiripuranthagan, S.; Radhakrishnan, R.; Durai, M.; Kumaravel, S.; Vembuli, T.; Kaleekkal, N.J. Fabrication of mesoporous TiO$_2$/PVDF photocatalytic membranes for efficient photocatalytic degradation of synthetic dyes. *J. Environ. Chem. Eng.* **2021**, *4*, 105776. [CrossRef]
5. Lishchynskyi, O.; Shymborska, Y.; Stetsyshyn, Y.; Raczkowska, J.; Skirtach, A.G.; Peretiatko, T.; Budkowski, A. Passive antifouling and active self-disinfecting antiviral surface. *Chem. Engineer. J.* **2022**, *446*, 137048. [CrossRef] [PubMed]
6. Shiraishi, F.; Ikeda, S.; Kamikariya, N. Photocatalytic decompositions of gaseous HCHO over thin films of anatase titanium oxide converted from amorphous in a heated air and in an aqueous solution of hydrogen peroxide. *Chem. Engineer. J.* **2009**, *148*, 234–241. [CrossRef]
7. Amano, F.; Prieto-Mahaney, O.O.; Terada, Y.; Yasumoto, T.; Shibayama, T.; Ohtani, B. Decahedral single-crystalline particles of anatase titanium(IV) oxide with high photocatalytic activity. *Chem. Mat.* **2009**, *21*, 2601–2603. [CrossRef]

8. Wei, Z.W.; Wei, X.C.; Zheng, Y.X.; He, D.Y. Self-combustion fabrication of anatase/rutile titanium oxides encapsulated in thin carbon shells and their photocatalytic performance. *Mater. Lett.* **2013**, *113*, 163–166. [CrossRef]

9. Tizazu, G.; Adawi, A.M.; Leggett, G.J.; Lidzey, D.G. Photopatterning, etching, and derivatization of self-assembled monolayers of phosphonic acids on the native oxide of titanium. *Langmuir* **2009**, *25*, 10746–10753. [CrossRef]

10. Murakami, N.; Kawakami, S.; Tsubota, T.; Ohno, T. Dependence of photocatalytic activity on particle size of a shape-controlled anatase titanium(IV) oxide nanocrystal. *J. Mol. Catal. A-Chem.* **2012**, *358*, 106–111. [CrossRef]

11. Shih, P.C.; Huang, C.H.; Chen, T.H.; Lai, L.W.; Lu, Y.S.; Liu, D.S. Enhancement on Photocatalytic Activity of an Amorphous Titanium Oxide Film with Nano-Textured Surface by Selective-Fluorination Etching Process. *Mater. Res. Bull.* **2014**, *52*, 177–182. [CrossRef]

12. Gainanova, A.A.; Kuźmicheva, G.M.; VasiĺEva, I.G. Nanosized low-temperature phase of titanium(IV) oxide with anatase and eta-phase structure: Composition, structure, and photocatalytic properties. *Russ. Chem. Bull.* **2018**, *67*, 1350–1363. [CrossRef]

13. Enesca, A.; Andronic, L.; Duta, A. The influence of surfactants on the crystalline structure, electrical and photocatalytic properties of hybrid multi-structured (SnO2, TiO$_2$ and WO3) thin films. *Appl. Surf. Sci.* **2012**, *258*, 4339–4346. [CrossRef]

14. Navabpour, P.; Ostovarpour, S.; Hampshire, J.; Kelly, P.; Verran, J.; Cooke, K. The effect of process parameters on the structure, photocatalytic and self-cleaning properties of TiO$_2$ and Ag-TiO$_2$ coatings deposited using reactive magnetron sputtering. *Thin Solid Films* **2014**, *571*, 75–83. [CrossRef]

15. Chen, J.Z.; Chen, T.H.; Lai, L.W.; Li, P.Y.; Liu, H.W.; Hong, Y.Y.; Liu, D.S. Preparation and characterization of the surface photocatalytic activity with NiO/TiO$_2$ nanocomposite structure. *Materials* **2015**, *8*, 4273–4286. [CrossRef]

16. Mandari, K.K.; Do, J.Y.; Vattikuti, S.V.P.; Police, A.K.R.; Kang, M. Solar light response with noble metal-free highly active copper(II) phosphate/titanium dioxide nanoparticle/copper(II) oxide nanocomposites for photocatalytic hydrogen production. *J. Alloy. Compd.* **2018**, *750*, 292–303. [CrossRef]

17. Mehr, M.E.; Maleki-Ghaleh, H.; Yarahmadi, M.; Kavanlouei, M.; Siadati, M.H. Synthesis and characterization of photocatalytic zinc oxide/titanium oxide (core/shell) nanocomposite. *J. Alloy. Compd.* **2021**, *882*, 160777. [CrossRef]

18. Lee, M.K.; Shih, T.H.; Shih, C.M. Highly visible photocatalytic activity of fluorine and nitrogen co-doped nanocrystalline anatase phase titanium oxide converted from ammonium oxotrifluorotitanate. *IEEE Trans. Nanotechnol.* **2007**, *6*, 316–319. [CrossRef]

19. Hu, C.C.; Hsu, T.C.; Kao, L.H. One-step cohydrothermal synthesis of nitrogen-doped titanium oxide nanotubes with enhanced visible light photocatalytic activity. *Int. J. Photoenergy* **2012**, *2012*, 391958. [CrossRef]

20. Lazaro-Navas, S.; Prashar, S.; Fajardo, M.; Gomez-Ruiz, S. Visible light-driven photocatalytic degradation of the organic pollutant methylene blue with hybrid palladium-fluorine-doped titanium oxide nanoparticles. *J. Nanopart. Res.* **2015**, *17*, 94. [CrossRef]

21. Huang, S.R.; Huang, P.J. Visible-light driven graphene oxide/titanium dioxide hydrogels for photocatalytic reduction of nitrite. *J. Environ. Chem. Eng.* **2021**, *10*, 106902. [CrossRef]

22. Oktay, B.; Kayaman-Apohan, N. Polydimethylsiloxane (PDMS)-based antibacterial organic-inorganic hybrid coatings. *J. Coat. Technol. Res.* **2013**, *10*, 785–798. [CrossRef]

23. Pereyra, A.M.; Gonzalez, M.R.; Rosato, V.G.; Basaldella, E.I. A-type zeolite containing Ag$^+$/Zn^{2+} as inorganic antifungal for waterborne coating formulation. *Prog. Org. Coat.* **2014**, *77*, 213–218. [CrossRef]

24. Ferraris, S.; Perero, S.; Costa, P.; di Confiengo, G.G.; Cochis, A.; Rimondini, L.; Renaus, F.; Verne, E.; Ferraris, M.; Spriano, S. Antibacterial inorganic coating on metallic surface for temporary fixation devices. *Appl. Surf. Sci.* **2020**, *508*, 144707. [CrossRef]

25. Stefanello, A.; Fracari, J.C.; Silva, M.; Lemos, J.G.; Garcia, M.V.; dos Santos, B.A.; Copetti, M.V. Influence of type, concentration, exposure time, temperature, and pressure of organic load on the antifungal efficacy of industrial sanitizers against Aspergillus brasiliensis (ATCC 16404). *Food Microbiol.* **2021**, *97*, 103740. [CrossRef]

26. Miao, R.Y.; Liu, H.; Lei, Q.; Zhong, L.L.; Zhang, L.; He, J.Z.; Ma, Z.H.; Yao, Y. Single-organic component g-C3.6N4 achieves superior photoactivity antibacterial. *Chem. Engineer. J.* **2022**, *440*, 35873. [CrossRef]

27. Hui, A.P.; Yang, F.F.; Yan, R.; Kang, Y.R.; Wang, A.Q. Palygorskite-based organic-inorganic hybrid nanocomposite for enhanced antibacterial activities. *Nanomaterials* **2022**, *11*, 3230. [CrossRef]

28. Tarimala, S.; Kothari, N.; Abidi, N.; Hequet, E.; Fralick, J.; Dao, L.L. New approach to antibacterial treatment of cotton fabric with silver nanoparticle-doped silica using sol-gel process. *J. Appl. Polym. Sci.* **2006**, *101*, 2938–2943. [CrossRef]

29. Kumar, V.; Jolivalt, C.; Pulpytel, J.; Jafari, R.; Arefi-Khonsari, F. Development of silver nanoparticle loaded antibacterial polymer mesh using plasma polymerization process. *J. Biomed. Mater. Res.* **2013**, *101*, 1121–1132. [CrossRef]

30. Khan, B.A.; Chevali, V.S.; Na, H.N.; Zhu, J.; Warner, P.; Wang, H. Process and properties of antibacterial silver nanoparticle-loaded hemp hurd/poly (lactic acid) biocomposites. *Compos. Pt. B-Eng.* **2016**, *100*, 10–18. [CrossRef]

31. Sheikh, F.A.; Kanjwal, M.A.; Kim, H.; Pandeya, D.R.; Hong, S.T.; Kim, H.Y. Fabrication of titanium oxide nanofibers containing silver nanoparticles. *J. Ceram. Process. Res.* **2010**, *11*, 685–691.

32. Song, D.H.; Uhm, S.H.; Kim, S.E.; Kwon, J.S.; Han, J.G.; Kim, K.N. Synthesis of titanium oxide thin films containing antibacterial silver nanoparticles by a reactive magnetron co-sputtering for application in biomedical implants. *Mater. Res. Bull.* **2012**, *47*, 2994–2998. [CrossRef]

33. Bian, H.; Zhang, Z.; Xu, X.; Gao, Y.; Wang, T. Photocatalytic activity of Ag/ZnO/AgO/TiO$_2$ composite. *Physica E* **2020**, *124*, 114236. [CrossRef]

34. Deekshitha, S.; Vidya, K. Solar light active biogenic titanium dioxide embedded silver oxide (AgO/Ag2O@TiO$_2$) nanocomposite structures for dye degradation by photocatalysis. *Mater. Sci. Semicond. Process.* **2021**, *132*, 105923. [CrossRef]

35. Kacprzyńska-Gołacka, J.; Łożyńska, M.; Barszcz, W.; Sowa, S.; Wieciński, P.; Woskowicz, E. Microfiltration membranes modified with composition of titanium oxide and silver oxide by magnetron sputtering. *Polymers* **2021**, *13*, 141. [CrossRef]

36. Thukkaram, M.; Cools, P.; Nikiforov, A.; Rigole, P.; Coenye, T.; Voort, P.V.D.; Laing, G.D.; Vercruysse, C.; Declercq, H.; Morent, R.; et al. Antibacterial activity of a porous silver doped TiO_2 coating on titanium substrates synthesized by plasma electrolytic oxidation. *Appl. Surf. Sci.* **2020**, *500*, 144235. [CrossRef]

37. Wu, C.Y.; Chiang, B.S.; Chang, S.; Liu, D.S. Determination of photocatalytic activity in amorphous and crystalline titanium oxide films prepared using plasma-enhanced chemical vapor deposition. *Appl. Surf. Sci.* **2011**, *257*, 1893–1897. [CrossRef]

38. Maier, S.A.; Atwater, H.A. Plasmonics: Localization and guiding of electromagnetic energy in metal/dielectric structures. *J. Appl. Phys.* **2005**, *98*, 011101. [CrossRef]

39. Willets, K.A.; Wan Duyne, R.P. Localized surface plasmon resonance spectroscopy and sensing. *Annu. Rev. Phys. Chem.* **2007**, *58*, 267–297. [CrossRef]

40. Xu, W.F.; Chin, C.C.; Hung, D.W.; Wei, P.K. Transparent electrode for organic solar cells using multilayer structures with nanoporous silver film. *Sol. Energy Mater. Sol. Cells* **2013**, *118*, 81–89. [CrossRef]

41. Zhang, S.G.; Zhang, X.W.; Yin, Z.G.; Wang, J.X.; Si, F.T.; Gao, H.L.; Dong, J.J.; Liu, X. Optimization of electroluminescence from n-ZnO/AlN/p-GaN light-emitting diodes by tailoring Ag localizer surface plasmon. *J. Appl. Phys.* **2012**, *112*, 013112. [CrossRef]

42. Mogensen, K.B.; Kneipp, K. Size-dependent shifts of plasmon resonance in silver nanoparticle films using controlled dissolution: Monitoring the onset of the surface screening effects. *J. Phys. Chem. C* **2014**, *118*, 28075–28083. [CrossRef]

43. Xu, Z.W.; Zhang, Y.K.; Chen, T.H.; Chang, J.H.; Lee, T.H.; Li, P.L.; Liu, D.S. Enhancement on the Surface Hydrophobicity and Oleophobicity of an Organosilicon Film by Conformity Deposition and Surface Fluorination Etching. *Materials* **2018**, *11*, 1089. [CrossRef]

44. Patakfalvi, R.; Papp, S.; Dékány, I. The kinetics of homogeneous nucleation of silver nanoparticles stabilized by polymers. *J. Nanopart. Res.* **2007**, *9*, 353–364. [CrossRef]

45. Ikramullah, A.; Thakur, A.; Salve, D.; Pai, G.; Rathore, M.; Joshi, D.S. Synthesis of homogenous colloidal silver nanoparticles. *J. Nanosci. Nanoengineer.* **2011**, *1*, 59–66.

46. Li, W.; Liang, R.; Hu, A.; Huang, Z.; Zhou, N. Generation of oxygen vacancies in visible light activated one-dimensional TiO_2 photocatalysts. *RSC Adv.* **2014**, *4*, 36959. [CrossRef]

47. Lanje, A.S.; Sharma, S.J.; Pode, R.B. Synthesis of silver nanoparticles: A safer alternative to conventional antimicrobial and antibacterial agents. *J. Chem. Pharm. Res.* **2010**, *2*, 478–483.

48. Zhang, F.; Wolf, G.K.; Wang, X.; Liu, X. Surface properties of silver doped titanium oxide films. *Surf. Coat. Technol.* **2001**, *148*, 65–70. [CrossRef]

49. Gao, X.Y.; Wang, S.Y.; Li, J.; Zheng, Y.X.; Zhang, R.J.; Zhou, P.; Yang, Y.M.; Chen, L.Y. Study of structure and optical properties of silver oxide films by ellipsometry, XRD and XPs methods. *Thin Solid Films* **2004**, *455*, 438–442. [CrossRef]

50. Lützenkirchen-Hecht, D.; Strehblow, H.H. Anodic silver (II) oxides investigated by combined electrochemistry, ex situ XPS and in situ X-ray absorption spectroscopy. *Surf. Interface Anal.* **2009**, *41*, 820–829. [CrossRef]

51. Vintsitskly, D.A.; Lazarev, M.K.; Kardash, T.Y.; Fedorova, E.A.; Slavinskaya, E.M.; Boronin, A.I. Mixed silver-nickel oxide $AgNiO_2$: Probing by CO during XPS study. *J. Chem. Phys.* **2020**, *132*, 044707.

52. Steveson, M.; Arora, P.S.; Smart, R.S.C. XPS studies of low-temperature plasma-produced graded oxide-silicate-silica layers on titanium. *Surf. Interface Anal.* **1998**, *26*, 1027–1034. [CrossRef]

53. Hashimoto, S.; Tanaka, A. Alteration of Ti 2p XPS spectrum for titanium oxide by low-energy Ar ion bombardment. *Surf. Interface Anal.* **2002**, *34*, 262–265. [CrossRef]

54. Lin, X.; Rong, F.; Fu, D.; Yuan, C. Enhanced photocatalytic activity of fluorine doped TiO_2 by loaded with Ag for degradation of organic pollutants. *Powder Technol.* **2012**, *219*, 173–178. [CrossRef]

55. Temperton, R.H.; Gibson, A.; O'Shea, J.N. In situ XPS analysis of the atomic layer deposition of aluminium oxide on titanium dioxide. *Phys. Chem. Chem. Phys.* **2019**, *21*, 1393–1398. [CrossRef]

56. Li, P.Y.; Liu, H.W.; Chen, T.H.; Chang, C.H.; Lu, Y.S.; Liu, D.S. Characterization of an Amorphous Titanium Oxide Film Deposited onto a Nano-Textured Fluorination Surface. *Materials* **2016**, *9*, 429–439. [CrossRef]

57. Barrère, F.; Lebugle, A.; Van Blitterswijk, C.A.; De Groot, K.; Layrolle, P.; Rey, C. Calcium phosphate interactions with titanium oxide and alumina substrates: An XPS study. *J. Mater. Sci.-Mater. Med.* **2003**, *14*, 419–425. [CrossRef]

58. Jin, Z.; Gao, H.; Hu, L. Removal of Pb(II) by nano-titanium oxide investigated by batch, XPS and model techniques. *RSC Adv.* **2015**, *5*, 88520. [CrossRef]

59. Ajmal, H.M.S.; Khan, F.; Ul Huda, N.; Lee, S.; Nam, K.; Kim, H.Y.; Eom, T.H.; Kim, S.D. High-performance flexible ultraviolet photodetectors with Ni/Cu-codoped ZnO nanorods grown on PET substrates. *Materials* **2019**, *9*, 1067. [CrossRef]

60. Ajmal, H.M.S.; Khan, F.; Nam, K.; Kim, H.Y.; Kim, S.D. Ultraviolet photodetection based on high-performance Co-plus-Ni doped ZnO nanorods grown by hydrothermal method on transparent plastic substrate. *Nanomaterials* **2020**, *10*, 1225. [CrossRef]

61. Li, H.; Zhao, G.; Han, G.; Song, B. Hydrophilicity and photocatalysis of $Ti_{1-x}V_xO_2$ films prepared by sol–gel method. *Surf. Coat. Technol.* **2007**, *201*, 7615–7618. [CrossRef]

62. Pathania, D.; Sharma, G.; Naushad, M.; Kumar, A. Synthesis and characterization of a new nanocomposite cation exchanger polyacrylamide Ce(IV) silicophosphate: Photocatalytic and antimicrobial applications. *J. Ind. Eng. Chem.* **2014**, *20*, 3596–3603. [CrossRef]

63. Gupta, V.K.; Sharma, G.; Pathania, D.; Kothiyal, N.C. Nanocoposite pectin Zr(IV) selenotungstophosphate for adsorptional/photocatalytic remediation of methylene blue and malachite green dye from aqueous system. *J. Ind. Eng. Chem.* **2015**, *21*, 957–964. [CrossRef]

64. Zhang, J.W.; Wang, S.; Liu, F.S.; Fu, X.J.; Ma, G.Q.; Hou, M.S.; Tang, Z. Preparation of defective TiO_{2-x} hollow microsphere for photocatalytic degradation of methylene blue. *Acta. Phys.-Chim. Sin.* **2019**, *35*, 885–895. [CrossRef]

65. Guo, L.; Okinaka, N.; Zhang, L.; Watanabe, S. Facile synthesis of ZnFe2O4/SnO2 composites for efficient photocatalytic degradation of methylene blue. *Mater. Chem. Phys.* **2021**, *262*, 124273. [CrossRef]

66. Dikici, T.; Demirci, S.; Tünçay, M.M.; Yildirim, B.K.; Kaya, N. Effect of heating rate on structure, morphology and photocatalytic properties of TiO_2 particles: Thermal kinetic and thermodynamic studies. *J. Sol.-Gel Sci. Technol.* **2021**, *97*, 622–637. [CrossRef]

67. Sarkandi, A.F.; Montazer, M.; Harifi, T.; Rad, M.M. Innovative preparation of bacterial cellulose/silver nanocomposite hydrogels: In situ green synthesis, characterization, and antibacterial properties. *J. Appl. Polym. Sci.* **2020**, *138*, 49824. [CrossRef]

68. Qing, Y.A.; Cheng, L.; Li, R.Y.; Liu, G.C.; Zhang, Y.B.; Tang, X.F.; Wang, J.C.; Liu, H.; Qin, Y.G. Potential antibacterial mechanism of silver nanoparticles and the optimization of orthopedic implants by advanced modification technologies. *Int. J. Nanomed.* **2018**, *13*, 3311–3327. [CrossRef]

69. Sabry, R.S.; Al-fouadi, A.H.A.; Habool, H.K. Enhanced antibacterial activity of anodic aluminum oxide membranes embedded with nano-silver-titanium dioxide. *J. Adhes. Sci. Technol.* **2018**, *32*, 874–888. [CrossRef]